Dual-color metal-induced and Förster resonance energy transfer for cell nanoscopy

Anna M. Chizhik[a,†], Carina Wollnik[a,†], Daja Ruhlandt[a], Narain Karedla[a,b], Alexey I. Chizhik[a], Lara Hauke[a], Dirk Hähnel[a], Ingo Gregor[a,b], Jörg Enderlein[a,b,*], and Florian Rehfeldt[a,*]
[a]Third Institute of Physics–Biophysics, University of Göttingen, 37077 Göttingen, Germany; [b]Center for Nanoscale Microscopy and Molecular Physiology of the Brain (CNMPB), 37077 Göttingen, Germany

ABSTRACT **We report a novel method, dual-color axial nanometric localization by metal-induced energy transfer, and combine it with Förster resonance energy transfer (FRET) for resolving structural details in cells on the molecular level. We demonstrate the capability of this method on cytoskeletal elements and adhesions in human mesenchymal stem cells. Our approach is based on fluorescence-lifetime-imaging microscopy and allows for precise determination of the three-dimensional architecture of stress fibers anchoring at focal adhesions, thus yielding crucial information to understand cell–matrix mechanics. In addition to resolving nanometric structural details along the *z*-axis, we use FRET to gain precise information on the distance between actin and vinculin at focal adhesions.**

Monitoring Editor
Patricía Bassereau
Institut Curie

Received: Jun 5, 2017
Revised: Jan 26, 2018
Accepted: Feb 6, 2018

INTRODUCTION

The *mechano*-induced differentiation of human mesenchymal stem cells (hMSCs) is an example where stress fibers and focal adhesions are key players of translating mechanical cues from the extracellular environment into biochemical signaling that leads to lineage decision (Engler *et al.*, 2006). It was shown that stress fiber structure critically depends on the mechanical interactions with the environment and is an early morphological marker for differentiation (Zemel *et al.*, 2010a,b; Paluch *et al.*, 2015). The coupling of stress fibers to focal adhesions became a widely studied topic in *mechano*-biology and the exact geometry of this architecture is important to deduce the acting forces. However, current studies, albeit even using superresolution in *x* and *y*, lack sufficient height information and therefore a detailed view on the three-dimensional (3D) architecture, essential to understand force transmission from and to the substrate, and to elucidate the *mechano*-sensing of cells. Particularly crucial for the mechanical coupling of the cell's cytoskeleton to the surrounding are focal adhesions, where vinculin plays an essential role (Geiger *et al.*, 2009; Case *et al.*, 2015; Burridge and Guilluy, 2016; Livne and Geiger, 2016).

There are several coherent optical microscopy methods such as reflection interference contrast microscopy (see, e.g., Limozin and Sengupta, 2009), or interferometric scattering microscopy (see, e.g., Kukura *et al.*, 2009), which routinely achieve nanometer and subnanometer localization accuracy of scattering/reflecting entities along the optical axis. However, these methods lack the specificity and, to some extent, the sensitivity of fluorescence microscopy methods. Over recent years, various fluorescence microscopy techniques for also gaining superresolution along the optical axis have been proposed and implemented. Within the context of stochastic optical reconstruction microscopy (STORM; Rust *et al.*, 2006) or photoactivated localization microsocopy (PALM; Betzig *et al.*, 2006), the most widely used techniques are astigmatic imaging (Huang *et al.*, 2008), biplane imaging (Juette *et al.*, 2008), or helical wavefront shaping (Pavani *et al.*, 2009). They all achieve localization accuracies of single molecules along the optical axis on the order of ~50 nm. Two distinct but powerful techniques, which are not based on single-molecule localization, are supercritical angle fluorescence imaging (Ruckstuhl and Verdes, 2004; Deschamps *et al.*, 2014), and variable-angle total internal reflection fluorescence microscopy (see,

This article was published online ahead of print in MBoC in Press (http://www.molbiolcell.org/cgi/doi/10.1091/mbc.E17-05-0314) on February 14, 2018.

†These authors contributed equally and should be considered as co–first authors.

J.E. and F.R. conceived and directed the study. A.M.C., C.W., A.I.C., and L.H. performed experiments. A.M.C., A.I.C., D.R., N.K., and I.G. analyzed the data. A.I.C., I.G., and D.H. developed the setup. All authors discussed the results. A.M.C., C.W., J.E., and F.R. wrote the paper, and all authors reviewed and edited the final version of the paper.

*Address correspondence to: Jörg Enderlein (jenderl@gwdg.de) and Florian Rehfeldt (rehfeldt@physik3.gwdg.de).

Abbreviations used: 3D, three-dimensional; BSA, bovine serum albumin; dcMIET, dual-color MIET imaging; FLIC, fluorescence interference contrast; FRET, Förster resonance energy transfer; hMSCs, human mesenchymal stem cells; iPALM, interferometric PALM; MIET, metal induced energy transfer; PALM, photoactivated localization microscopy; PBS, phosphate-buffered saline; PL, photoluminescence; STORM, stochastic optical reconstruction microscopy; TCSPC, time-correlated single-photon counting.

© 2018 Chizhik, Wollnik, *et al.* This article is distributed by The American Society for Cell Biology under license from the author(s). Two months after publication it is available to the public under an Attribution–Noncommercial–Share Alike 3.0 Unported Creative Commons License (http://creativecommons.org/licenses/by-nc-sa/3.0).
"ASCB®," "The American Society for Cell Biology®," and "Molecular Biology of the Cell®" are registered trademarks of The American Society for Cell Biology.

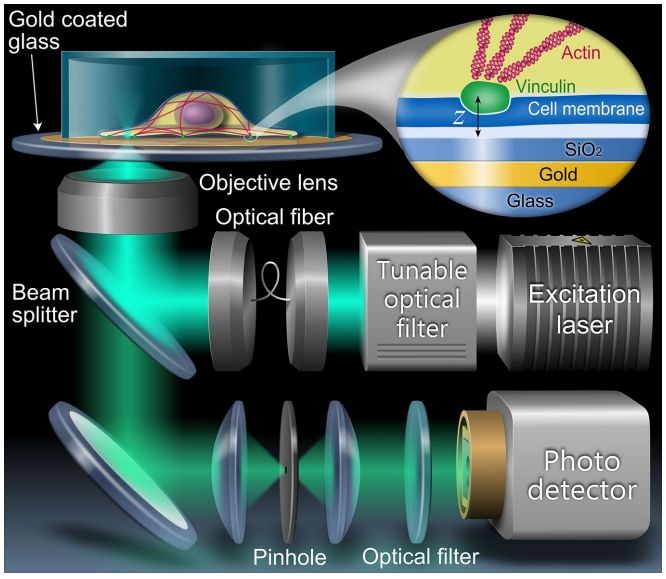

FIGURE 1: Schematic of the setup for dcMIET. The inset shows the anchoring of actin stress fibers to ensembles of the focal adhesion protein vinculin. The measured height *z* is always counted from the top of the SiO_2-spacer.

e.g., Stock *et al.*, 2003, and Dos Santos *et al.*, 2016). They achieve, under optimal conditions, an axial resolution around 10 nm. Along the same line, there is a class of methods based on fluorescence interference contrast (FLIC), initially developed by Braun and Fromherz (1997), and recently further improved as variable incidence angle FLIC (Ajo-Franklin et al., 2005) and scanning angle interference microscopy (Paszek *et al.*, 2012). Although the last one also achieves subnanometer precision, all of these techniques require the use of optically opaque silicon wafers with a precisely controlled silicon oxide layer, and for the latter two an extremely accurate tuning of the angle of incidence.

One class of techniques which indeed achieves single nanometer localization accuracy along the optical axis is represented by interferometric PALM (iPALM) or 4pi-STORM (Shtengel *et al.*, 2009; Aquino *et al.*, 2011). Using iPALM with a plethora of constructed photoactivatable fluorescent proteins fused to focal adhesion proteins in U2OS cells, it was possible to localize different proteins in the focal adhesion cluster with a resolution of 10 nm to 15 nm along the *z*-axis (Kanchanawong *et al.*, 2010). However, complex instrumentation, requirement of specialized fluorescent protein fusion constructs (photoactivatable fluorescent proteins), and double transfection of cells render this method rather tedious and complicated.

Here, we present a novel method of height and colocalization measurements of two dyes in cells with nanometer accuracy. We used MIET imaging (Chizhik *et al.*, 2014), which allows us to measure the axial localization of a fluorophore with an accuracy of ~3 nm in both living and fixed cells. Additionally, we extended our setup with a second fluorescence emission channel that allows for dual-color MIET imaging (dcMIET) and Förster resonance energy transfer (FRET) measurements (see Figure 1).

The principle of MIET imaging is based on the energy transfer from a fluorescent molecule to surface plasmons within a thin metal film on a glass surface, which results in the acceleration of its deexcitation rate. This can be observed as a reduction of the molecule's fluorescence lifetime (Karedla *et al.*, 2014). Because, within the first 200 nm, the energy transfer rate is monotonically dependent on the distance of a molecule from the metal layer, the fluorescence lifetime can be directly converted into a distance between the emitter and the metal surface within this distance range (see Supplemental Figure S3).

Here, for the first time, we present a detailed description of dcMIET and its combination with FRET imaging. This allows us to measure the axial localization of both actin filaments and vinculin, and additionally to monitor their distance within FRET range (<10 nm). By combining the capabilities of dcMIET and FRET microscopy, we achieve unprecedented axial resolution and demonstrate their applicability to elucidate the 3D structure of actin and vinculin at focal adhesions in hMSCs.

RESULTS

To study the developing actomyosin stress fiber structure and the architecture of focal adhesions, we fixed hMSCs at distinct time points after seeding, and fluorescently stained actin (Atto 647N-phalloidin) and vinculin (Atto 488/anti-mouse/anti-vinculin; see *Materials and Methods* for further details). Figure 2 shows a time series of developing actin stress fibers starting at heights of >150 nm in the early regime (1–6 h). Later, from 12 h on, they form tight connections to focal adhesions at low distances to the substrate (~40 nm), and finally span throughout the cell (increasing above 180 nm). For better visualization, the height-profile images are weighted by fluorescence intensity to reflect the amount of actin within the stress fibers.

For a detailed view of the 3D architecture of stress fibers and focal adhesions, we imaged selected areas using dcMIET with reduced pixel size. Because we labeled the two structures with dyes that constitute a FRET pair, we can also measure the distance between actin and vinculin at the adhesion sites. However, one needs to be careful when analyzing the vinculin height using MIET, because FRET also affects the lifetime of this fluorophore (acting as FRET donor). For an undisturbed measurement of the vinculin height, we

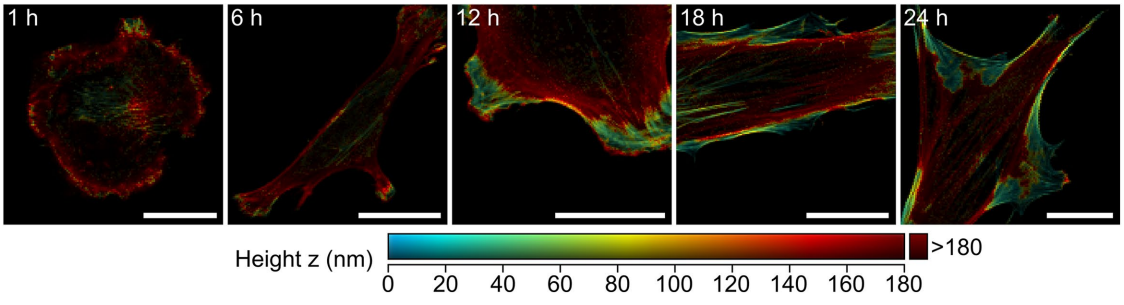

FIGURE 2: Time series of actin height imaged by MIET. Intensity-weighted height images of actin filaments stained with Atto 647N-phalloidin in human mesenchymal stem cells (hMSCs) fixed on gold-coated coverslips at 1 h ($N = 8$ cells), 6 h ($N = 11$), 12 h ($N = 10$), 18 h ($N = 6$), and 24 h ($N = 27$) after seeding. Scale bar is 30 µm.

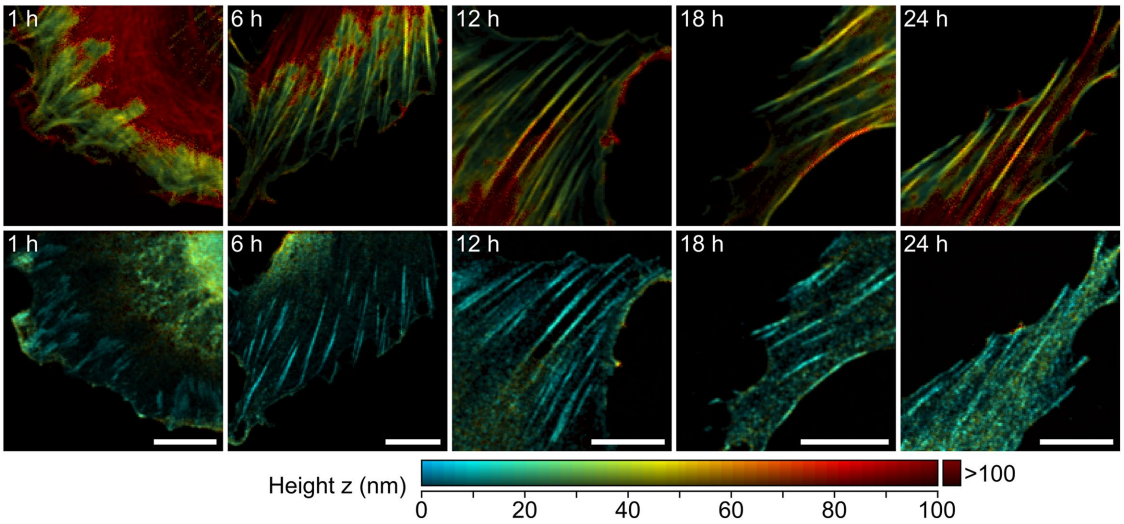

FIGURE 3: Time series of dual-color MIET imaging of actin and vinculin. Intensity-weighted height images of actin (top row) and vinculin (bottom row) focal adhesions for the same cell areas. Cells were fixed on gold-coated coverslips at 1 h ($N = 4$), 6 h ($N = 3$), 12 h ($N = 4$), 18 h ($N = 4$), and 24 h ($N = 7$) (from left to right) after seeding. Scale bar is 10 µm.

completely bleached the actin fluorophore (the FRET acceptor) before performing MIET measurements and analysis. Figure 3 illustrates the temporal maturation of focal adhesions. In particular, it shows how actin filaments develop into stress fibers and move closer to the substrate over time.

The growing focal adhesions show that the height of the vinculin ensembles above the surface is smaller than the height of the actin ensembles, which is in agreement with the standard picture of stress fibers anchoring at focal adhesions, as was also shown with iPALM (Kanchanawong *et al.*, 2010). During the early phase of adhesion (1 –6 h) vinculin is close to the surface (11 ± 2 nm), and during maturation and growth of the focal adhesions this value increases to 19 ± 5 nm after 24 h (see Supplemental Figure S4). When analyzing vinculin in seven different cells, we get an average height of (20 ± 8) nm at 24 h (see Supplemental Figure S6). This height coincides well with the height of paxillin where we observed 17 ± 19 nm (see Supplemental Figure S7).

With the height information of actin within stress fibers, and of vinculin as an integral part of the focal adhesion, we are now able to draw a detailed 3D picture of stress fiber anchoring as depicted in Figure 4. Here, we analyzed the obtained height information along selected actin filaments and the associated vinculin complex after 12 and 24 h. Although the vinculin height remains more or less constant (~10–15 nm above the substrate), the actin filaments exhibit an inclination toward the surface. Over their first several micrometers, they increase by ~20–30 nm, which corresponds to a very shallow inclination angle of 0.15 ± 0.01° and 0.18 ± 0.04° for three fibers at 12 and 24 h, respectively (see Figure 4). Remarkably, we observe a gap in height between the "centers of mass" of the ensembles of actin and vinculin that decreases from roughly 20 nm at 12 h to 10 nm at 24 h, which is indicative of the maturation of stress fiber anchoring at focal adhesions.

After having measured and analyzed the distinct 3D architecture of actin and vinculin using MIET, we use the same experimental system with uncoated glass coverslips to measure FRET for determining the distance between the two proteins. For obtaining quantitative FRET values, we performed donor lifetime measurements before and after acceptor bleaching (see Supplemental Figures S1, S2, and S5; Jares-Erijman and Jovin, 2003, 2006; Beutler *et al.*, 2008). Figure 5 shows the temporal evolution of the distance between the two proteins. Although the focal adhesion areas were growing, there was no significant change in the mean distance during a time span from 6 to 24 h. Here, FRET data reveal the proximity between F-actin from stress fibers and vinculin in focal adhesions that is stable throughout the maturation process. Furthermore, we observed that FRET occurs not in all focal adhesions, and that some focal adhesions show FRET only within distinct small areas, which shows the complexity and heterogeneity of these supramolecular structures. For Figure 5, we have selected only cells where the mean values of the lifetime difference of the vinculin label before and after acceptor bleaching is larger than the SD of the lifetime values.

DISCUSSION

Our results show that dcMIET is a powerful method to spatially resolve the *z*-positions of two different dye-labeled proteins (actin and vinculin) in cells. By combining it with FRET, we obtained additional insight into the 3D structure of the anchoring of stress fibers at focal adhesions. The analysis of the temporal evolution of actin heights as shown in Figure 2 nicely illustrates how the actin filaments move closer to the surface while the cell is spreading and firmly adhering. Although the fibers are distributed over a broad height range during an early phase (1–6 h), their distance to the surface reduces around 12 h and later time points (to ~40 nm). We could also successfully demonstrate that it is possible to quantitatively disentangle the effects of MIET and FRET on the donor lifetime, so that we could measure distances of two different molecules from a surface, and their mutual distance from each other. Using dcMIET, we confirmed the standard picture of stress fibers attached to focal adhesions, and could also observe that vinculin is below the actin filaments. Moreover, during maturation of focal adhesion complexes, vinculin aggregates grow larger as indicated by an increase in height and SD, and the mean height of the actin bundles above the surface is decreasing. The measured values for vinculin height above the substrate (19 ± 5 nm) are within the range of previously published values where vinculin was only slightly higher than the plasma membrane (90–106 nm vs. ~100 nm; Paszek *et al.*, 2012, 2014), or roughly 22.7 ± 5.5 nm higher than the membrane as iPALM measurements suggest (Kanchanawong *et al.*, 2010). The nanometer-precise height information along the fibers and of the vinculin clusters shown in Figure 3 gives us a detailed picture of stress fibers anchoring at focal

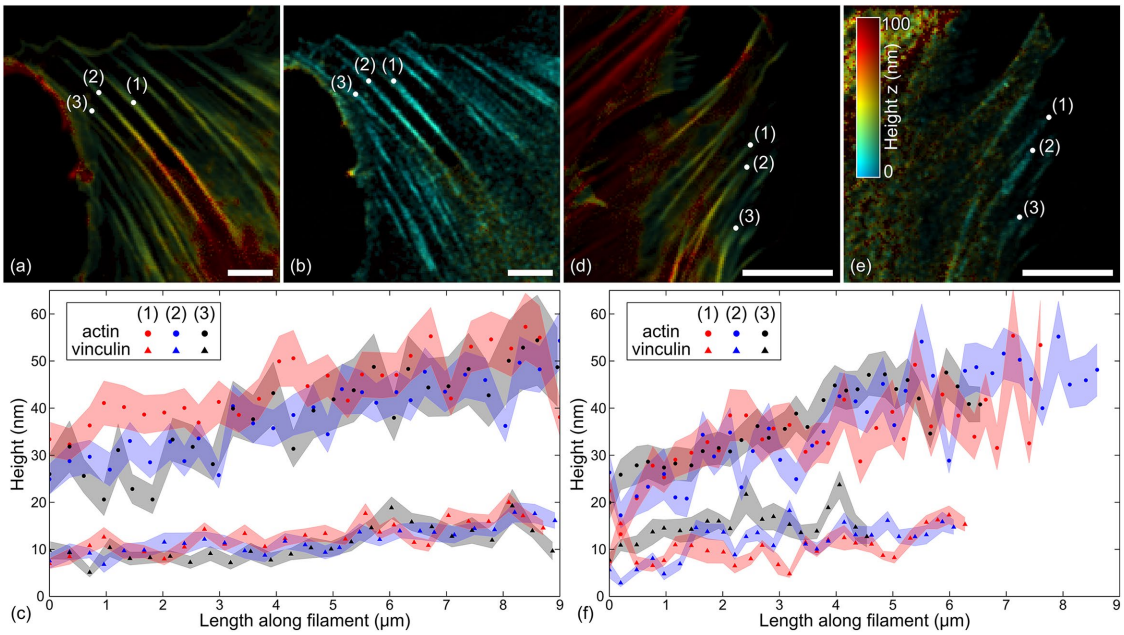

FIGURE 4: 3D architecture of stress fibers at focal adhesions changes from 12 to 24 h. Height profiles along actin filaments and vinculin complexes after 12 and 24 h. Images a and b correspond to intensity-weighted ensemble heights of actin and vinculin, respectively, for a cell fixed 12 h after seeding. Images d and e correspond to intensity-weighted ensemble heights of actin and vinculin, respectively, for a cell fixed 24 h after seeding. White points (1), (2), and (3) on the intensity-weighted height images indicate the starting points of the height profiles shown in images c and f. They show the height of actin filaments (circles) and vinculin clusters (triangles) at the same focal adhesion. The shaded areas mark the 1σ-regions of the height values. Scale bar is 10 μm.

adhesions and spanning the cell at a slight inclination of below 1°. Although we observe a gap of roughly 10–20 nm between actin and vinculin at focal adhesions, the FRET data shows a close proximity of both proteins of ~7 nm. This latter distance is based on a Förster radius of 5.0 nm (see *Materials and Methods*). However, it is unlikely that vinculin and actin form stoichiometric complexes at focal adhesions. Instead, there are many more labels at the actin fibers than at the vinculin site. Therefore, the FRET donor can interact with multiple acceptor dyes. For such arrangements, the transfer rates add up, and a considerably larger effective Förster radius should be used (Maliwal *et al.*, 2012). Thus, the FRET-determined distance has to be considered as a lower bound. In summary, the combination of dcMIET and FRET is a powerful method to dissect and elucidate the detailed 3D structure of molecular architecture within cells (e.g., nuclear envelope, synaptic vesicles, exocytosis, and endocytosis) that will be very helpful for many structural aspects of the basal part of the cell.

Our method of combined dcMIET and FRET imaging in biological cells is a straightforward and versatile tool for elucidating the 3D architecture of molecular structures. It can be easily implemented in standard fluorescence lifetime microscopes. In contrast to other existing axial superresolution techniques, it does not require specialized fluorescent labels, and it is compatible with commercially available

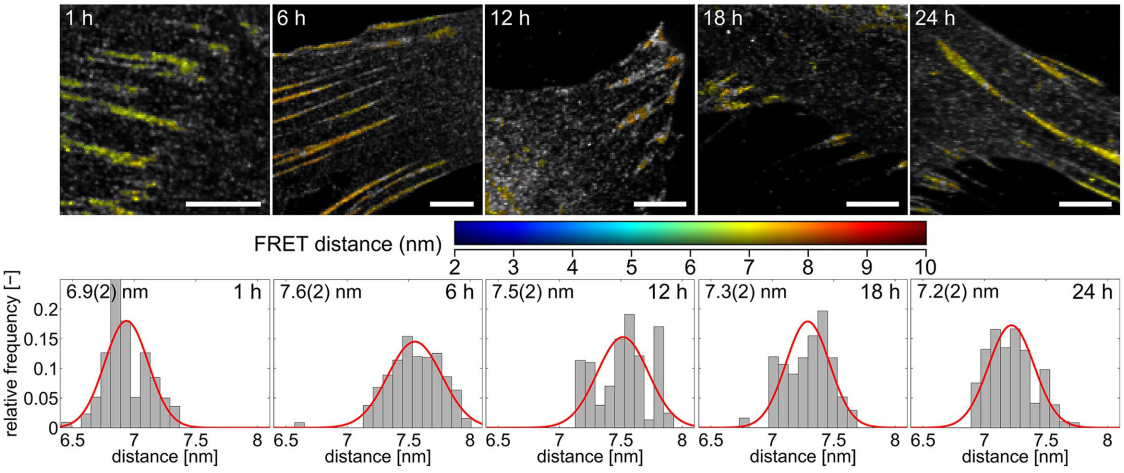

FIGURE 5: Constant FRET distance of actin and vinculin over time. Images show the color coded FRET distance between actin and vinculin in focal adhesions overlaid on the intensity image of vinculin (after bleaching of Atto 647N-phalloidin). As can be seen, this distance does not significantly change over time as imaged 1 h ($N = 4$ cells), 6 h ($N = 4$), 12 h ($N = 5$), 18 h ($N = 4$), and 24 h ($N = 6$) after seeding. Scale bar is 5 μm.

dyes and antibodies. In particular, our method can also be used with fluorescent fusion proteins, thus allowing for live cell measurements. Concerning focal adhesions, our results confirm the standard picture of stress fibers anchoring at focal adhesions that maturate within the first 24 h and show that stress fibers are slightly inclined and above the vinculin complexes. Although we focused in this study on actin and vinculin, dcMIET with FRET can also be used to study other structures in cells within the first 150 nm from the basal membrane.

MATERIALS AND METHODS

Experimental setup

Photoluminescence (PL) measurements of cells on gold were performed with a homebuilt confocal microscope equipped with an objective lens of high numerical aperture (Apo N, 60× oil, 1.49 NA; Olympus Europe, Hamburg, Germany). A pulsed, linearly polarized white light laser (SC400-4-20; Fianium, UK; pulse width ~50 ps, repetition rate 20 MHz) equipped with a tunable filter (AOTFnC- 400.650-TN; Pegasus Optik GmbH, Wallenhorst, Germany) served as excitation source, delivering light with a tunable wavelength of 488 or 635 nm. The light was reflected by a nonpolarizing beam-splitter toward the objective, and the backscattered excitation light was blocked with long-pass filters (EdgeBasic BLP01-488R; Semrock, New York, for the green channel, and BLP01-635R; Semrock, New York, for the red channel). An additional band-pass filter 550/88 (BrightLine FF01-550/88; Semrock, New York) was used for the vinculin (Atto 488) measurements. Emission light was focused onto the active area of an avalanche photodiode (PDM Series; MicroPhoton Devices), and data recording was performed with a multichannel picosecond event timer (HydraHarp 400; PicoQuant GmbH, Berlin, Germany).

Samples were scanned with a focused laser spot using a piezo nano-positioning stage (P-562.3CD; Physik Instrumente GmbH, Karlsruhe, Germany). PL spectra of Atto 488 and Atto 647N molecules inside the cells were recorded using a spectrograph (SR 303i; Andor Technology, Belfast, UK) equipped with a charge-coupled device camera (iXon DU897 BV; Andor Technology, Belfast, UK). For measurement without FRET, the FRET acceptor (Atto 647N-phalloidin labeling actin) was bleached with a diode laser (MRL-FN-639, CNI laser; CNI Optoelectronics Tech., Changchun, People's Republic of China) at 640 nm excitation (laser power is ~1 mW after the objective lens). Bleaching time was typically around 10 min per cell.

For MIET measurements, glass cover slides were coated with the following multilayer structure: 3 nm Ti, 15 nm Au, 3 nm Ti, 20 nm SiO_2. The metal and silica films were prepared by vapor deposition onto a cleaned glass cover slide (thickness 170 µm) using an electron beam source (Univex 350; Leybold) under high-vacuum conditions (~10^{-6} mbar). During vapor deposition, film thickness was monitored using an oscillating quartz unit, and afterward verified by atomic force microscopy.

For FRET measurements, "donor-acceptor" images were first acquired by exciting the donor molecules present on the vinculin protein with the diode laser at 485 nm. Subsequently, the fluorescent dyes used for labeling actin filaments were bleached using the diode laser at 640 nm excitation with a power of ~140 µW after the objective lens. The bleaching time usually was around 10 min per area. Thereafter, "donor only" images were acquired on the same area using the 485 nm excitation.

Metal nanocavity for quantum yield measurements

The nanocavity used for quantum yield measurements consists of two silver mirrors with subwavelength spacing. The bottom silver mirror was prepared by vapor deposition of a 30 nm silver film (see above for details) onto a commercially available cleaned microscope glass coverslip (thickness 170 µm). The top silver mirror was prepared by vapor deposition of a 60-nm-thick silver film onto the surface of a plano-convex lens (focal length of 150 mm) under the same conditions.

The spherical shape of the upper mirror allowed for reversibly tuning the cavity length by moving the laser focus laterally away or toward the contact point between the lens and the cover slide. It should be noted that across the size of the diffraction-limited laser focus, the cavity can be considered to be a plane-parallel resonator. For a detailed presentation of the theoretical background, refer to Chizhik *et al.* (2013).

The measured quantum yield of Atto 488/anti-mouse/anti-vinculin/3% bovine serum albumin (BSA) in phosphate-buffered saline (PBS) solution is $\Phi_0 = 0.67$. The free space fluorescence lifetime of this sample is $\tau_0 = 2.9$ ns.

Fluorescence lifetime data evaluation

Both for dcMIET and FRET measurements, fluorescence photons were detected in time-tagged, time-resolved mode. Each photon carries two time tags, one with respect to the start of the experiment, which is counted as the number of preceding laser pulses, and a second with respect to the last laser pulse. Additionally, line change markers from the piezo driver are recorded as "virtual photons" which are used for recognizing a change of lines in the scan image, and for sorting the photons into individual pixels based on their arrival time in each line. By calculating histograms of the arrival times of the sorted photons with respect to the last laser pulses, one obtains time-correlated single-photon counting (TCSPC) curves for each individual pixel. In this way, one obtains intensity and lifetime information for all pixels of an image. One limitation of FLIM with TCSPC and single-photon detectors is that the photon count rate should not exceed some threshold (typically 1% of the laser excitation rate) to prevent data distortion due to pileup and detector/electronics dead-times. Measuring at high count rates introduces severe distortions into the acquired TCSPC and intensity data. We determined the detector and electronics dead-times as 74 and 80 ns, respectively, as described in Isbaner *et al.* (2016). These values were then used in the correction algorithm to obtain dead-time corrected TCSPC curves. We then calculated the decay with a least-square-error minimization algorithm using a multiexponential tail fitting model. All lifetime values presented in this paper are always the inverse of the average decay rate extracted from these fits. Furthermore, the dead-time correction algorithm also yielded corrected intensity values in each pixel. To estimate the lifetime uncertainties needed for determining the height uncertainties in Figure 3, we performed both simulations and bootstrapping of experimental data. We found the empirical formula $\sigma_\tau \approx 4.8\tau/\sqrt{N}$, where τ is the lifetime and N the number of photons. To avoid large fitting errors at low photon numbers, only pixels with at least 1000 photons were evaluated.

Cell culture

Adult hMSCs from bone marrow (Lonza Group, Basel, Switzerland; #PT-2501), were cultured in T75 cell culture flasks (Corning; 43061) in DMEM (Life Technologies, Thermo Fisher Scientific, Waltham, MA; A18967-01) supplemented with 10% fetal bovine serum (Sigma-Aldrich, St. Louis, MO; F2442-500ML) and 1% antibiotics (penicillin/streptomycin; Life Technologies, Thermo Fisher Scientific, Waltham, MA; 15140-122) at 37°C and 5% CO_2 and passaged every 2–3 d (passage #4 was used in this study). Cells were seeded on 25 mm glass and gold-coated glass coverslips at a density of 10.000 hMSCs per glass in six-well plates (Sarstedt AG & Co., Nuembrecht, Germany; 83.3920) with 2 ml growth medium per well and grown at

37°C and 5% CO_2. Cells were chemically fixed 1, 6, 12, 18, and 24 h after seeding in 10% formaldehyde (Sigma-Aldrich, St. Louis, MO; 47608-250ML-F) in PBS for 5 min. Subsequently, cells were permeabilized using 0.5% Triton X-100 (Carl Roth GmbH & Co. KG, Karlsruhe, Germany; 6683.1) in PBS for 10 min and blocked with 3% BSA (Sigma-Aldrich, St. Louis, MO; A9418-100G) in PBS for 30 min, incubated again with Triton X for 5 min and thoroughly washed with PBS. All antibodies were kept in a 3% BSA PBS solution. Immunostaining was performed with anti-vinculin (Sigma-Aldrich, St. Louis, MO; V9131-.2ML) (1:1000) for 1 h, then anti-mouse immunoglobulin G (IgG) Atto 488 (Sigma-Aldrich, St. Louis, MO; 62197) (1:500) for 1 h, and then phalloidin Atto 647N (ATTO-TEC GmbH, Siegen, Germany; AD647N-82) (1:250) for 1.5 h. Paxillin was stained using a primary anti-paxillin antibody (abcam; ab32084) (1:100) for 21 h followed by an anti-rabbit IgG Atto 488 (Sigma-Aldrich, St. Louis, MO; 40839) for 2.5 h.

Samples were mounted on microscope slides (VWR; 631-1550) using Fluoroshield mounting medium (Sigma-Aldrich, St. Louis, MO; F6182-20ML).

Wide-field fluorescence images were obtained with an Axio Observer.Z1 microscope (Zeiss, Oberkochen, Germany; 431007-0001-000), using a 20× objective (Zeiss, Oberkochen, Germany; 1006-591) and a sCMOS camera (Andor Technology, Belfast, Northern Ireland; Zyla 4.2).

ACKNOWLEDGMENTS

This work was supported in part by the Deutsche Forschungsgemeinschaft (DFG) through the Cluster of Excellence "Center for Nanoscale Microscopy and Molecular Physiology of the Brain (CNMPB)." A.M.C. is grateful to the Human Frontiers Science Program Organization for financial support under Grant no. RGP0061/2015. A.I.C. and D.R. are grateful to the DFG for financial support via SFB 937 (project A14). N.K. is grateful to the DFG for financial support of his position via SFB 860 (project A06). F.R. acknowledges funding by the DFG through SFB 755 (project B8), SFB 937 (project A13), and the Niedersachsen-Israel framework (MWK-VWZN2722).

REFERENCES

Ajo-Franklin CM, Ganesan PV, Boxer SG (2005). Variable incidence angle fluorescence interference contrast microscopy for *Z*-imaging single objects. Biophys J 89, 2759–2769.

Aquino D, Schönle A, Geisler C, v Middendorff C, Wurm CA, Okamura Y, Lang T, Hell SW, Egner A (2011). Two-color nanoscopy of three-dimensional volumes by 4Pi detection of stochastically switched fluorophores. Nat Methods 8, 353–359.

Betzig E, Patterson GH, Sougrat R, Lindwasser OW, Olenych S, Bonifacino JS, Davidson MW, Lippincott-Schwartz J, Hess HF (2006). Imaging intracellular fluorescent proteins at nanometer resolution. Science 313, 1642–1645.

Beutler M, Makrogianneli K, Vermeij RJ, Keppler M, Ng T, Jovin TM, Heintzmann R (2008). satFRET: estimation of Förster resonance energy transfer by acceptor saturation. Eur Biophys J 38, 69–82.

Braun D, Fromherz P (1997). Fluorescence interference-contrast microscopy of cell adhesion on oxidized silicon. Appl Phys A 65, 341–348.

Burridge K, Guilluy C (2016). Focal adhesions, stress fibers and mechanical tension. Exp Cell Res 343, 14–20.

Case LB, Baird MA, Shtengel G, Campbell SL, Hess HF, Davidson MW, Waterman CM (2015). Molecular mechanism of vinculin activation and nanoscale spatial organization in focal adhesions. Nat Cell Biol 17, 880–892.

Chizhik AI, Gregor I, Ernst B, Enderlein J (2013). Nanocavity-based determination of absolute values of photoluminescence quantum yields. Chem Phys Chem 14, 505–513.

Chizhik AI, Rother J, Gregor I, Janshoff A, Enderlein J (2014). Metal-induced energy transfer for live cell nanoscopy. Nat Photon 8, 124–127.

Deschamps J, Mund M, Ries J (2014). 3D superresolution microscopy by supercritical angle detection. Opt Express 22, 29081–29091.

Dos Santos MC, Déturche R, Vézy C, Jaffiol R (2016). Topography of cells revealed by variable-angle total internal reflection fluorescence microscopy. Biophys J 111, 1316–1327.

Engler AJ, Sen S, Sweeney HL, Discher DE (2006). Matrix elasticity directs stem cell lineage specification. Cell 126, 677–689.

Geiger B, Spatz JP, Bershadsky AD (2009). Environmental sensing through focal adhesions. Nat Rev Mol Cell Biol 10, 21–33.

Huang B, Wang W, Bates M, Zhuang X (2008). Three-dimensional super-resolution imaging by stochastic optical reconstruction microscopy. Science 319, 810–813.

Isbaner S, Karedla N, Ruhlandt D, Stein SC, Chizhik A, Gregor I, Enderlein J (2016). Dead-time correction of fluorescence lifetime measurements and fluorescence lifetime imaging. Opt Express 24, 9429–9445.

Jares-Erijman EA, Jovin TM (2003). FRET imaging. Nat Biotech 21, 1387–1395.

Jares-Erijman EA, Jovin TM (2006). Imaging molecular interactions in living cells by FRET microscopy. Curr Opin Chem Biol 10, 409–416.

Juette MF, Gould TJ, Lessard MD, Mlodzianoski MJ, Nagpure BS, Bennett BT, Hess ST, Bewersdorf J (2008). Three-dimensional sub–100 nm resolution fluorescence microscopy of thick samples. Nat Methods 5, 527–529.

Kanchanawong P, Shtengel G, Pasapera AM, Ramko EB, Davidson MW, Hess HF, Waterman CM (2010). Nanoscale architecture of integrin-based cell adhesions. Nature 468, 580–584.

Karedla N, Chizhik AI, Gregor I, Chizhik AM, Schulz O, Enderlein J (2014). Single-molecule metal-induced energy transfer (smMIET): resolving nanometer distances at the single-molecule level. Chem Phys Chem 15, 705–711.

Kukura P, Ewers H, Muller C, Renn A, Helenius A, Sandoghdar V (2009). High-speed nanoscopic tracking of the position and orientation of a single virus. Nat Methods 6, 923–927.

Limozin L, Sengupta K (2009). Quantitative reflection interference contrast microscopy (RICM) in soft matter and cell adhesion. Chem Phys Chem 10, 2752–2768.

Livne A, Geiger B (2016). The inner workings of stress fibers—from contractile machinery to focal adhesions and back. J Cell Sci 129, 1293–1304.

Maliwal BP, Raut S, Fudala R, D'Auria S, Marzullo VM, Luini A, Gryczynski I, Gryczynski Z (2012). Extending Förster resonance energy transfer measurements beyond 100 Å using common organic fluorophores: enhanced transfer in the presence of multiple acceptors. J Biomed Opt 17, 0110061–0110068.

Paluch EK, Nelson CM, Biais N, Fabry B, Moeller J, Pruitt BL, Wollnik C, Kudryasheva G, Rehfeldt F, Federle W (2015). Mechanotransduction: use the force(s). BMC Biol 13, 1–14.

Paszek MJ, DuFort CC, Rossier O, Bainer R, Mouw JK, Godula K, Hudak JE, Lakins JN, Wijekoon AC, Cassereau L, *et al.* (2014). The cancer glycocalyx mechanically primes integrin-mediated growth and survival. Nature 511, 319–325.

Paszek MJ, DuFort CC, Rubashkin MG, Davidson MW, Thorn KS, Liphardt JT, Weaver VM (2012). Scanning angle interference microscopy reveals cell dynamics at the nanoscale. Nat Methods 9, 825–827.

Pavani SRP, Thompson MA, Biteen JS, Lord SJ, Liu N, Twieg RJ, Piestun R, Moerner W (2009). Three-dimensional, single-molecule fluorescence imaging beyond the diffraction limit by using a double-helix point spread function. Proc Natl Acad Sci USA 106, 2995–2999.

Ruckstuhl T, Verdes D (2004). Supercritical angle fluorescence (SAF) microscopy. Opt Express 12, 4246–4254.

Rust MJ, Bates M, Zhuang X (2006). Sub-diffraction-limit imaging by stochastic optical reconstruction microscopy (STORM). Nat Methods 3, 793–796.

Shtengel G, Galbraith JA, Galbraith CG, Lippincott-Schwartz J, Gillette JM, Manley S, Sougrat R, Waterman CM, Kanchanawong P, Davidson MW (2009). Interferometric fluorescent super-resolution microscopy resolves 3D cellular ultrastructure. Proc Natl Acad Sci USA 106, 3125–3130.

Stock K, Sailer R, Strauss W, Lyttek M, Steiner R, Schneckenburger H (2003). Variable-angle total internal reflection fluorescence microscopy (VA-TIRFM): realization and application of a compact illumination device. J Microsc 211, 19–29.

Zemel A, Rehfeldt F, Brown AEX, Discher DE (2010a). Cell shape, spreading symmetry, and the polarization of stress-fibers in cells. J Phys Condens Matter 22, 194110.

Zemel A, Rehfeldt F, Brown AEX, Discher DE, Safran SA (2010b). Optimal matrix rigidity for stress-fibre polarization in stem cells. Nat Phys 6, 468–473.